Powder Technology 425 (2023) 118610

Contents lists available at ScienceDirect

Powder Technology

journal homepage: www.journals.elsevier.com/powder-technology

Tracking of Marangoni driven motion during laser powder bed fusion

Bryce Cox [a,*], Milad Ghayoor [a,b], Somayeh Pasebani [a,b], Joshua Gess [a]

[a] School of Mechanical, Industrial and Manufacturing Engineering, Oregon State University, Corvallis, OR, 97330, United States of America
[b] Advanced Technology and Manufacturing Institute (ATAMI), Corvallis, OR 97330, United States of America

HIGHLIGHTS

- Change in position for neutrally buoyant particles with varying initial locations tracked.
- Marangoni number related to change in nondimensional enthalpy.
- Enthalpies indicate a transition region between conduction mode and keyhole type melting.
- Increasing the magnitude of surface tension coefficient resulted in increased Marangoni flow.

GRAPHICAL ABSTRACT

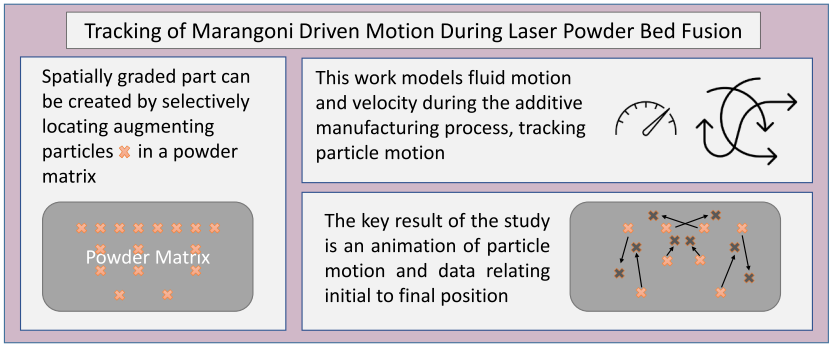

ARTICLE INFO

Keywords:
Numerical simulation
Laser powder bed fusion
Marangoni
Functionally graded
Metal matrix composite
Melt pool

ABSTRACT

Laser Powder Bed Fusion (LPBF) can be used to create Functionally Graded Materials (FGMs) by selectively distributing property augmenting particles throughout the build matrix. With this method parts can be created with nonhomogeneous properties tuned to spatially varied, pre-determined design constraints. To unlock this capability, the fluid motion that occurs in the molten liquid phase must be thoroughly understood. More importantly, the actual tracking of motion during the LPBF process is needed. A numerical model of heat transfer and fluid flow in LPBF process was created. Using results from the model the motion of particles starting at many different locations was tracked. The average change in position for these particles based on starting location was calculated. The effects of non-dimensional parameters on melt pool size were examined. These results were validated experimentally and compared to what is available in the literature.

1. Introduction

Additive Manufacturing (AM) can produce complex, custom parts with reduced waste, reduced need for costly tooling, and fewer limitations when compared to traditional manufacturing techniques [1]. Laser powder bed fusion (LPBF), also known as selective laser melting (SLM) is a process commonly used to create additively manufactured metal parts by distributing a thin layer of metal powder over a substrate. A laser then passes over the powder, selectively melting targeted areas dictated by the design intent for the part. An additional layer of powder is then added, and the laser passes again. The process is repeated as a part is made, layer by layer. The flexibility and complexity in the design of a

* Corresponding author.
E-mail address: coxbry@Oregonstate.edu (B. Cox).

https://doi.org/10.1016/j.powtec.2023.118610
Received 29 November 2022; Received in revised form 17 March 2023; Accepted 30 April 2023
Available online 2 May 2023

part allowed by the LPBF process provide an opportunity for significant advancement in multiple industries, as parts can be customized in shape and function for specific needs [2]. These benefits can be compounded by introducing nonhomogeneous properties tuned to pre-determined design constraints that are spatially varied. These Functionally Graded Materials (FGMs) can be formed by selectively distributing property augmenting particles throughout the build matrix [3]. This allows for both the physical shape of the part and the functional performance of the part to be custom designed for each unique situation. For example, thermal conductivity augmenting particles can be selectively distributed within a heat sink to produce optimal thermal pathways for heat to be rejected from an underlying non-isoflux temperature/heating profile. In addition, FGMs can be used to improve the performance of orthopedics, heat shields, and heat engine components [4–6]. It is possible to create FGMs using LPBF, but it requires numerous additional steps, most notably the time-consuming ball-milling process [7]. Work is being done on developing a method of using ink jetting to selectively apply particles during the LPBF process, but it has not yet published.

The addition of reinforcing particles in the metal powder for the LPBF process has been shown to be effective at modifying the mechanical characteristics of the resulting part [8,9]. This has the potential to provide significant power to designers and allows for ultimate creativity in engineering problem solving. Solutions can be created that fit both the exact shape and performance needed for the purpose. However, there is currently a significant roadblock that must be overcome before LPBF can be used to create pre-designed FGMs. In order to design parts with properties that vary spatially to meet specific demand requirements, the path that additive particles take during the LPBF process must be known. This information is not available in the existing literature.

Results from numerous numerical simulations of LPBF and related laser welding processes have been published that provide details on process optimization, effects of varying laser power and scanning speed, and the related impacts to quality of the created part [10–17]. There are also many studies in literature that provide insight on the complex dynamics in a melt pool that must be understood to predict melt pool motion. Siao and Wen studied the primary contributors to molten metal motion in LPBF [18], and saw that the two drivers of melt pool motion are buoyancy and Marangoni stress. They found that the effects on fluid motion from buoyancy were small when compared to the Marangoni flow in LPBF. They also provided information on the general direction of flow created by Marangoni stress. Other studies also provide data for velocity and expected flow patterns in LPBF [19–23]. Khairallah et al. [24] developed a mesoscopic model that offers data on melt pool formation dynamics, along with temperature and velocity information for the LPBF process. These studies provide valuable information on flow dynamics and provide a clear picture of what is happening in the melt pool. However, additional information is necessary to design FGMs with selectively placed particles, and that is to track and predict the motion of these particles.

Experimental measurements have been taken to help fill in this information gap. Tenner et al. used high-speed cameras to measure velocity inside the keyhole created in laser welding [25]. Clark et al. used X-ray radiography to track tungsten carbide seed particles as they moved in a melt pool during the LPBF process [26]. Their work provides a 2-D view of the particles' locations over time. Kawahito et al. [27] used three-dimensional X-ray transmission to capture melt flow velocity, also using tracer particles. Guo et al. [28] used tungsten tracer particles and X-ray imaging to create images of instantaneous liquid flow direction in multiple planes that demonstrate the expected melt pool dynamics.

Creating functionally graded materials using LPBF can be done by adding material property enhancing particles to specific locations in the powder bed. But to achieve these enhanced properties at the desired locations in the finished part, there must be an understanding of how the particles will flow through the weld pool during formation, which can be provided by the discussed literature. What is not available are explicit paths particles would take from initial to final locations during LPBF.

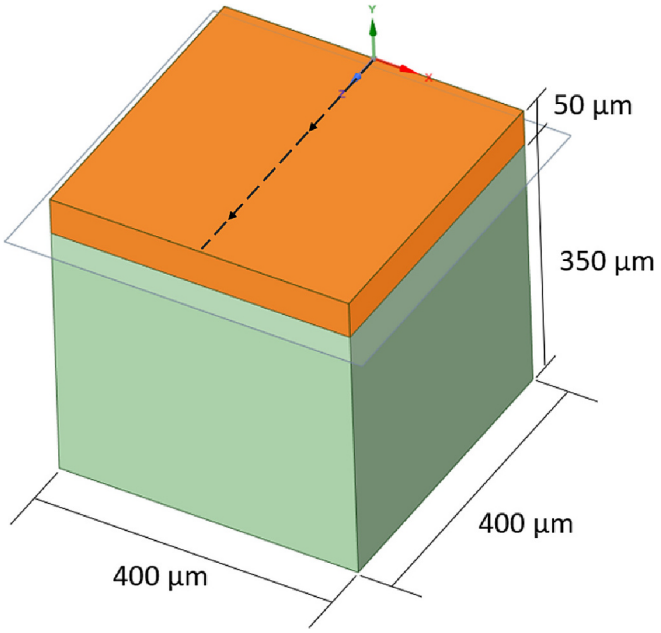

Fig. 1. Geometry and coordinate system of the volume modeled and laser path.

Due to the high temperature gradients, gradients in density are created that cause buoyancy driven flow. The high temperature gradients also create gradients in surface tension in the molten metal. These gradients in surface tension cause a Marangoni stress that induces circulatory motion in the melt pool. Only when designers can relate the initial location of an augmenting particle to the final location in the built part, taking into account the effects of buoyancy and more importantly Marangoni stress driven flow, can FGMs be possible with this process. However, current literature lacks the information necessary to enable the creation of spatially varied metal matrix composite (through adding reinforcement particles onto a metallic matrix) and functionally graded parts with LPBF. Only when the path of these additive particles can be predicted for the entire LPBF process, can educated decisions be made about where to apply these particles to achieve desired part properties and performance. The novelty of this work is to provide this vital information by developing a thermal-fluid model that predicts hydrodynamic movement within the melt pool, i.e., circulatory Marangoni flow. The study will examine the magnitude of the induced Marangoni flow that is created with varying laser power input. This flow information is then used with a Lagrangian reference frame to track the motion of particles from multiple starting locations in the powder bed. By understanding where the particles reside prior to cooling, along with how they get to this terminal point, manufacturing engineers will be informed as to where the augmenting particles should be placed initially to yield the desired distribution of properties within the final part. This will ultimately shift the paradigm to manufacturing for design.

2. Materials and methods

2.1. Model development

A numerical model of the LPBF process was created using ANSYS Fluent on the ANSYS Workbench platform, version 2022 R1. A double precision transient model was developed to represent a single laser pass over a 50 µm depth of 316 L stainless steel powder that is located over a solid 316 L build plate (substrate). Fig. 1 shows a cube with length, depth, and width of 400 µm, which is the geometry used in the model, with the laser path marked with the dashed line. The orange area represents the powder, and the green represents the solid substrate. The centerline of the model is located at the line x = 0. The laser moves in the

positive z direction along this centerline.

The calculation was set up to run using built in options in Fluent. The maximum Reynolds number of the molten 316 L was expected to be <30 due low velocities and high viscosity values typical in molten metal, so a laminar viscous calculation method was used (it was later verified after model development that the maximum Reynolds number was indeed <30). The energy equation calculation was enabled in the software to include heat transfer in the model. The solver option selected in Fluent for pressure-velocity coupling was the SIMPLE scheme with Rhie-Chow distance-based flux. For the pressure spatial discretization selection in the software, the PRESTO! method was used. The momentum and energy equations both used second order upwind scheme options. The convergence criteria for continuity and velocities were that the residuals needed to be below 1×10^{-3}, and for the energy equation the residuals needed to reduce to below 1×10^{-6}. The under-relaxation factors used to achieve convergence were 0.1 for pressure, 0.25 for density, 1 for body forces, 0.1 for momentum, 0.25 for liquid fraction, and 1 for energy. To model the phase change, the enthalpy-porosity model for solidification and melting was used with a mushy zone parameter of 1×10^{7}. This is within the range recommended by the ANSYS user guide and was selected from that range because it gave results that best matched the experimental data.

The heat transfer boundary conditions for the top surface included convection and radiation exchange with ambient conditions at 293 K. The flow boundary condition on the top surface was dictated by the Marangoni stress. The flow boundary conditions for all sides and the bottom surface was the no slip condition. The heat transfer boundary condition for the sides parallel to the laser path were a constant temperature at 293 K, as they were expected to have minimal heat transfer. The laser passes through the other sides, and they were expected to have significant heat transfer. The boundary condition for these sides was a conductive heat flux calculated using the local surface temperature and an assumed ambient temperature of 293 K at a location far out into the powder bed (well outside the modeled volume). The bottom side also had this conductive heat flux boundary condition.

To ensure grid independent results, the model was run multiple times with a decreasing grid size. Temperature values were taken from the model results at 3 different depths in the melt pool, and the change in these temperatures were tracked with the decreasing grid size. It was found that decreasing the grid size below 7.6×10^{-6} m resulted in <1% change in all three temperature measurements, so this was the grid size used for simulations. Since this is a transient simulation the effect on timestep size was also examined. It was found that for the higher scanning speed to be used in the study (200 mm/s) a timestep of 5×10^{-5} s was required to avoid changes in temperature >1%. For the slower laser speed (100 mm/s) a timestep of 1×10^{-4} s was small enough to avoid impacts to the temperature results.

To model the heat provided by the laser, a user defined function (UDF) was created so that the energy provided can appropriately vary in space and time. The distribution of heat flux occurring inside the laser beam was represented with a simplified Gaussian model, $q_L^{''}(x,z) = q_0^{''} exp\left(\frac{-r^2}{r_0^2}\right)$ [29] where $q_L^{''}$ is the laser flux that hits the surface of the powder bed at the location x,z inside the radius of the laser beam. A separate model was used to estimate the penetration of this heat flux into the powder bed, $q^{''}(x,y,z) = q_L^{''}(x,z) * 0.9909 \exp(-6791y)$. This model that gives the applied laser flux based on location in the laser beam and distance into the powder bed was developed from data published by Wang et al. on the absorptivity of metal powders [30]. The UDF developed uses this model along with the laser speed to calculate the current laser location and the corresponding applied laser power in the powder bed. After initial testing it was found that at laser powers over 100 W the laser penetration did not result in a melt pool shape that was sufficiently similar to the experimental results. Therefore, at these higher laser powers the laser energy penetration deep in the powder bed was slightly increased. This resulted in better match in the shape and area of the melt pools.

Table 1
Material properties for materials used in experimental validation and as model inputs.

Property	Value	Reference
Apparent density of 316 L powder	4427.2 kg/m3	This work
Absorptivity of powder	0.6	Trapp et al. [31]
Particles Size distribution	D10: 18 μm, D50: 30 μm, D90: 49 μm	This Work
Emissivity of 316 L powder[1]	0.6	Gunther et al. [32]
Emissivity of molten 316 L	0.28	Fukuyama et al. [33]
Viscosity	0.05 kg/ms	[[34] Xiao]
Specific heat of 316 L powder[2]	$0.1097 + (3.174 \times 10^{-5}T)$ cal/g	[35,36]
Specific heat of molten 316 L	0.184 cal/g	Kim [36]
Density of molten 316 L[3]	$7.4327 + ((3.9338 \times 10^{-5}T) - (1.8007 \times 10^{-7}T^2))$ g/m^3	Kim [36]
Thermal Conductivity of 316 L powder[3]	0.016 T + 8.5961 w/mk	Cox et al. [37]
Thermal Conductivity of molten 316 L[2]	$124.1 + (3279 \times 10^{-5}T)$ w/mk	Kim [36]
Convective heat transfer coefficient	10 w/m^{2}k	Zhang et al. [38]
Laser beam diameter	40 μm	
Laser power	50, 75, 100, 125, 150 watts	
Laser scanning speed	100, 200 mm/s	

[1] Value for slightly oxidized 316 L powder at elevated temperature, only used for radiation exchange with ambient surroundings, laser absorption uses a more sophisticated model described in above.
[2] T is in units of Kelvin.
[3] T is in units of degree Celsius.

Table 1 lists the material properties that were used in the simulation, as well as properties for the 316 L powder that was used in the model validation experiments that will be discussed in the next section.

At the laser powers and speeds used in this study, some amount of vaporization of the stainless-steel powder was expected. To quantify this in the numerical model, Langmiur's equation for evaporation was used to estimate the evaporative mass flux $J_i = P_i^0 \sqrt{\frac{M_i}{2\pi RT}}$ where M_i is the molar mass, R is the universal gas constant, T is the temperature, P_i^0 is the vapor pressure, and J_i is the evaporative mass flux [18]. The vapor pressure was found using data from Chawla et al. [39] that relates temperature to the vapor pressure of molten 316 L. The model was initially run without vaporization, and the resulting temperatures were then used to find the vapor pressure and the resultant evaporative mass flux. This mass flux was then used to calculate the resulting energy that goes toward vaporization by multiplying the mass flux by the heat of vaporization.

2.2. Model validation

In order to provide confidence in the model, experimental samples were created for comparison to model results. Single-track samples were created using ORLAS Creator LPBF machine equipped with a continuous wave Yb: YAG fiber laser (wavelength of 1067 nm) and a stainless-steel build plate. To maintain a constant layer thickness throughout the whole experiment, a groove with the dimensions of 12 mm in length, 200 μm in width, and 50 μm in depth, representing a typical LPBF layer thickness, has been micromachined into the 316 L build plate. Then, the 316 L powder was spread on top of the groove to fill the groove, and then manually with the aid of a razor blade, a smooth surface on the top of the groove was achieved. Afterward, the laser beam, previously has been aligned with the center of the groove, hit the metal powder and deposited the melt track at the bottom of the groove.

Samples were created using laser power settings of 50, 75, 100, 125,

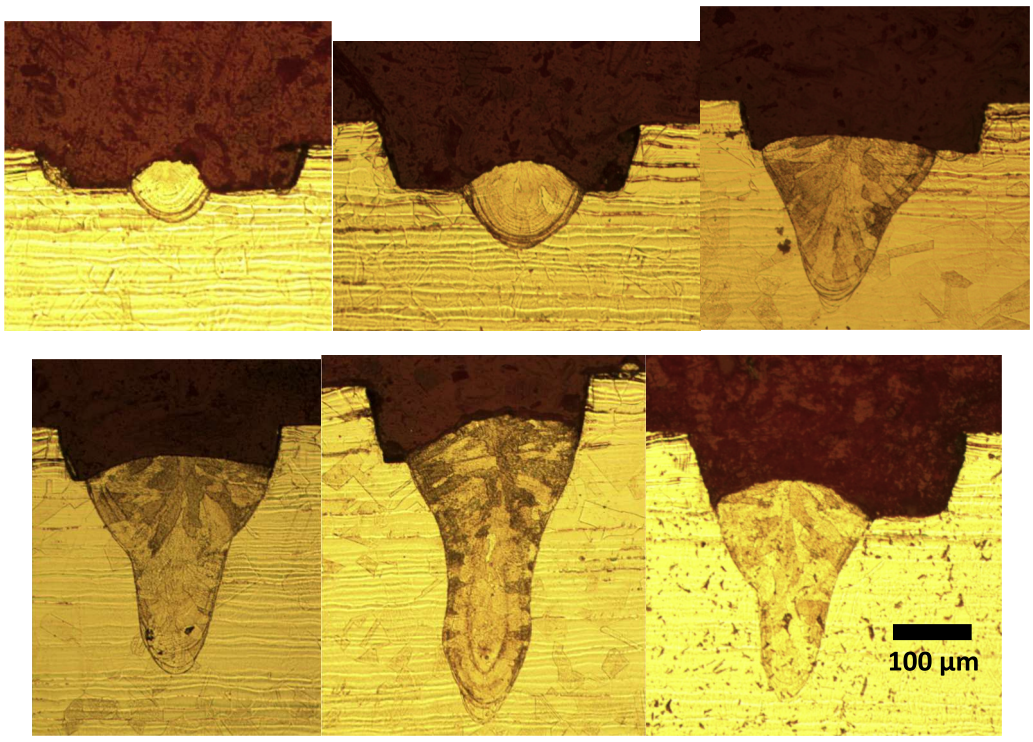

Fig. 2. Optical Micrographs of single track melt pools, top from left to right: 50 W 100 mm/s, 75 W 100 mm/s, 100 W 100 mm/s, bottom from left to right: 125 W 100 mm/s, 150 W 100 mm/s, 150 W 200 mm/s.

Table 2
Number of manufactured samples at each condition to be used for model validation.

Laser power						
		50 W	75 W	100 W	125 W	150 W
Scanning speed	100 mm/s	5	5	5	5	5
	200 mm/s	5	5	5	5	10

Table 3
Modeling results for melt pool dimensions for each test case.

	Laser power					
	Speed	50 W	75 W	100 W	125 W	150 W
Pool Width (microns)	200 mm/s	45.6	76	121.6	136.8	167.2
	100 mm/s	76	121.6	182.4	212.8	228
Pool Depth (microns)	200 mm/s	45.6	91.2	129.2	152	220.4
	100 mm/s	83.6	136.8	205.2	228	243.2
Pool Area (square microns)	200 mm/s	1502	4274	7451	10,166	16,519
	100 mm/s	3812	8779	18,137	21,718	24,606

and 150 W and laser scanning speed of the of 100 mm/s and 200 mm/s. Laser melting was performed in a nitrogen atmosphere, keeping the oxygen level in the build chamber <100 ppm to minimize oxidation. The deposited single tracks were sectioned along the perpendicular direction to the laser scanning track (parallel to the build direction). To reveal the melt pool boundaries in optical microscopy, the samples were mounted and polished following the standard metallography procedure and before the examination, and were electro-etched using a solution of 10 wt% oxalic acid and 90 wt% deionized water, applying 15 V DC for 15 s.

Fig. 2 shows the images that were taken of the samples manufactured for comparison to the modeling results. Multiple samples were created for each case and several measurements of melt pool width and depth were taken. The number of samples taken for each case are listed in Table 2. Imaging and area measurements were only done for the samples manufactured at speed of 100 mm/s and for the sample manufactured at laser power of 150 W and 200 mm/s.

The completed numerical model was run for the same cases as the experimental samples, and the melt pool width, depth, and cross-sectional area (in the x-y plane) were calculated. The predicted results are listed in Table 3. Fig. 3 shows images of the melt pool cross-sections for each of the cases from the model. Figs. 4 and 5 compare these modeling results with the experimental measurements in terms of melt pool width and melt pool depth, respectively.

A comparison of modeled results for melt pool width and experimental data is shown in Fig. 4. All of the modeled values for melt pool width fall within 10% of the average of the experimental values for each case, except for samples manufactured at laser power of 50 and 75 W at 200 mm/s. The melt pool depth shows some degree of agreement, but due to the significant variability in the depth measurement of the experimental samples, the experimental and modeled depths are not as close. The range of variation from experimental values of width varies from 1 to 55%. The deviation of simulated values from experimental values in this study fall within the range of other similar studies. Xiao and Zhang published data varying from experimental values in the range of 6–40% [34]. The simulated data from Siao and Wen showed variation of 8–107% for melt pool width and depth with varying laser power.

It was also important that the model provide agreement with experimental results for the shape of the melt pool. This was examined by comparing the cross-sectional area measurements of the modeled melt pools and those from the experiments. Melt pool area measurements were taken for each of the cases at 100 mm/s laser speed, and at 150 W laser power for the 200 mm/s speed. The results for both the modeled and the measured areas are shown in the plot in Fig. 6.

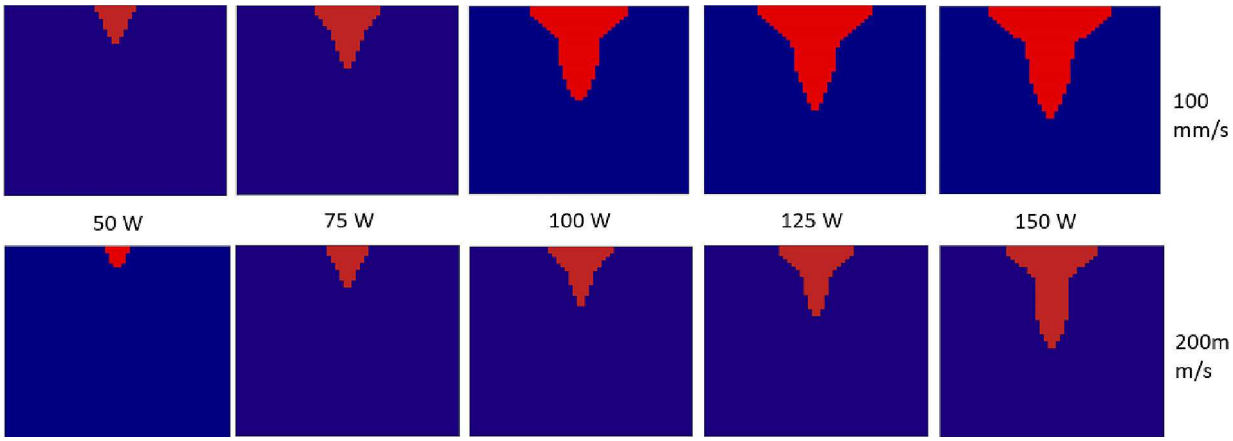

Fig. 3. Melt pool cross-sections predictions from modeling results for the samples listed in Table 3.

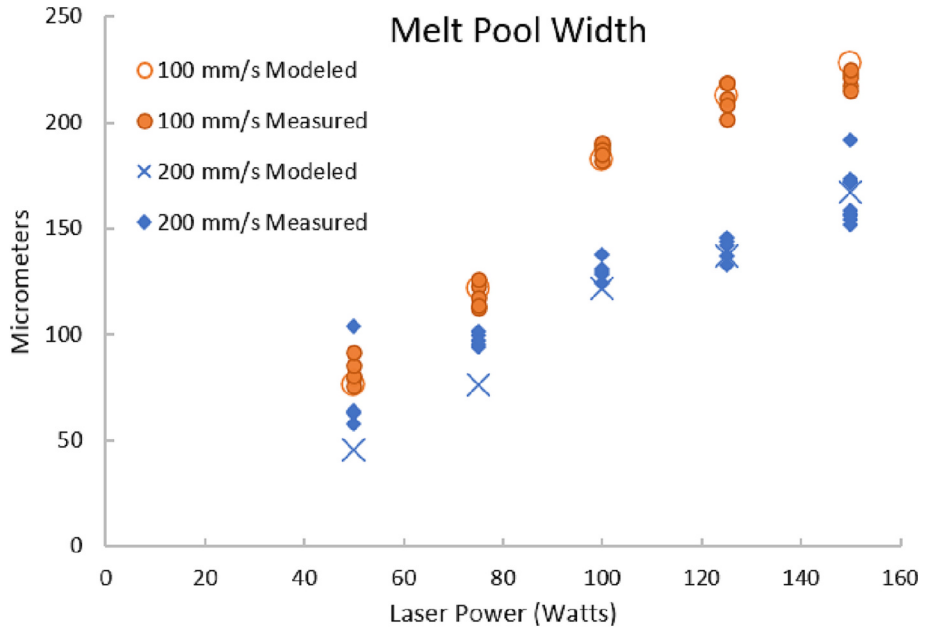

Fig. 4. Validation of melt pool width predicted by model with experimental measurements.

3. Results and discussion

Volumetric energy density (VED) was calculated for each case using a well-accepted method with $VED = \frac{P}{u\,h\,LT}$, where P is the laser power, u is the scanning speed, h is the hatch spacing, and LT is the powder layer thickness [40]. The volumetric energy density is dependent on the hatch spacing, which is the spacing between multiple laser passes. This work, however, was done all with single track cases with no repeated laser passes. Since there is no hatch spacing for single passes, the diameter of the laser beam was used in place of the hatch spacing. Table 4 shows the volumetric energy density for each case. Uddin et al. [41] did work on LPBF of 316 L stainless steel. Their values of VED vary from 45 to 83 J/mm^3. When using the same hatching spacing used by Uddin et al. (rather the laser beam diameter as was used in calculating the values in Table 4), the volumetric energy densities from this study fall in the range of 42–250 J/mm^3, showing that the values for heat input in this study are reasonable. The values listed in Table 4 are higher than this range because the laser beam diameter used in calculating the VED is much smaller than hatch spacing used by Uddin et al.

Because VED dependent on hatching spacing, (which is not a parameter in this study) VED may not be the best parameter to capture the energy input LPBF. Zhao et al. [42] also discuss the limitations of volumetric energy density as a metric for comparing different LPBF cases. More useful and widely applicable results could be found using a non-dimensional parameter to represent the combined effects of laser scanning speed and laser power. King et al. [43] used a ratio of enthalpies to represent input power in LPBF. The ratio is shown in eq. 1, where ΔH is the enthalpy per unit volume, h_s is the enthalpy of the molten metal at the melting temperature, A is absorptivity, P is the laser power, D is the thermal diffusivity, u is the laser speed, rho is the density, c is the specific heat, u is the laser scanning speed, T_m is the melting temperature, and sigma is the laser beam radius.

$\frac{\Delta H}{h_s} = \frac{AP}{\rho c T_m \sqrt{\pi D u \sigma^3}}$ (1) [43].

The above ratio allows for comparisons of multiple cases in a common way, so that the energy input into the powder bed, for example, a laser power of 100 W and a laser speed of 200 mm/s can easily be compared to an input of 125 W laser power and 100 mm/s. This is useful as the laser power might vary, but because of differing scanning speeds the powder bed might receive the same amount of energy, in which case it would be reasonable to expect some similarity in results.

Another parameter that will be used in the analysis of results in this study is the Marangoni number. The Marangoni number is a dimen-

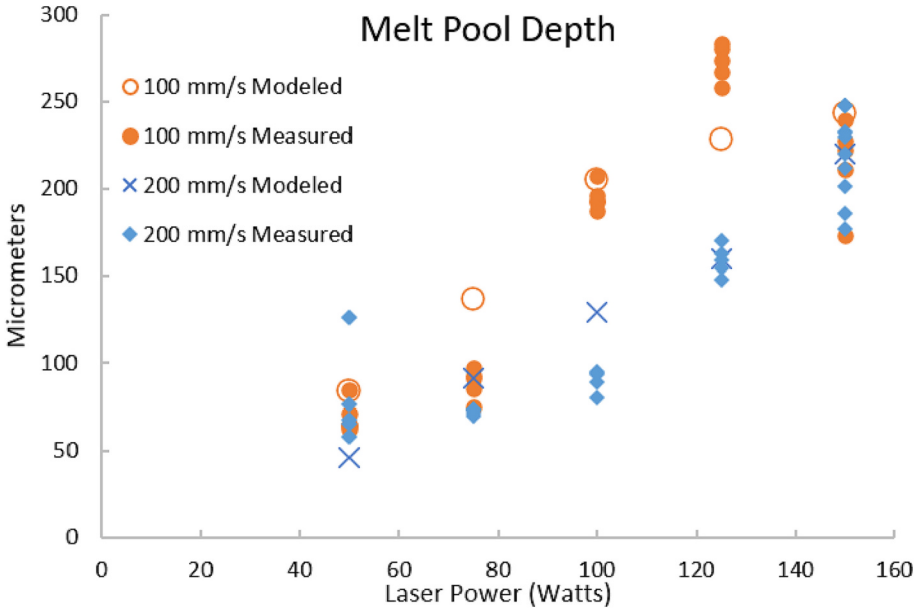

Fig. 5. Validation of melt pool depth predicted by the model with experimental measurements.

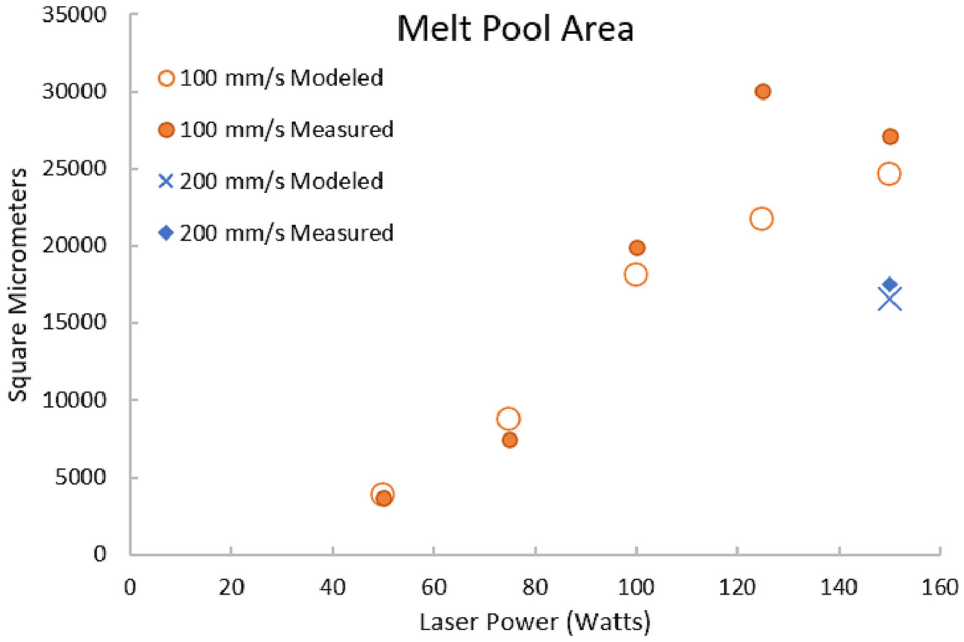

Fig. 6. Validation of melt pool cross-sectional areas predicted by the model with experimental measurements.

Table 4
Volumetric energy density (J/mm^3).

	100 mm/s	200 mm/s
50 W	250.0	125.0
75 W	375.0	187.5
100 W	500.0	250.0
125 W	625.0	312.5
150 W	750.0	375.0

sionless parameter that represents the ratio of surface tension forces to viscous forces in a flow. Eq. 2 gives the traditional representation of the Marangoni number where dγ/dT is the sensitivity of the surface tension gradient to temperature, w is the melt pool width (the characteristic length), μ is the dynamic viscosity, ΔT is the difference between the maximum pool temperature and the solidus temperature, and D is the thermal diffusivity.

$$Ma = -\frac{d\gamma}{dT}\frac{w\Delta T}{\mu D} \tag{2}$$

In this study, a simplification of the Marangoni number is used. The Marangoni number is calculated with the simplification that $u \approx -\frac{d\gamma}{dT}\frac{\Delta T}{\mu}$. Basically, this is assuming that all of the velocity in the x-direction comes from gradients in surface tensions. This is a simplification because some of the velocity in the x-direction will be induced from buoyancy-driven flow. To examine this assumption the model results for the case of 150 W laser power and 100 mm/s scanning speed were compared to running the same case in the model with no surface tension gradient (dγ/dT was

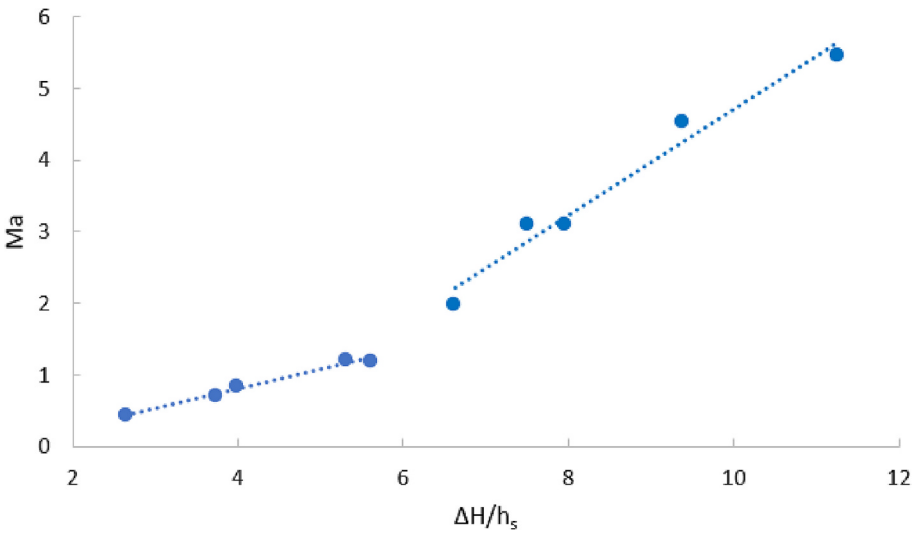

Fig. 7. $\Delta H/ h_s$ versus Marangoni number.

set to zero). The resulting maximum velocity for the case with surface tension gradients was 16 times larger than the velocity when surface tension gradients were turned off. With the magnitude of the velocity created by Marangoni effects being so much larger than those created by buoyancy, this was considered a reasonable simplification. Siao and Wen [18] found that the velocities induced from surface tension gradients were larger in magnitude than those from buoyancy. With this justification the following simplified Marangoni number was used (which is a specialized version of the Peclet number):

$$Ma = \frac{uw}{D} \tag{3}$$

In this form the Marangoni number also represents the ratio of convective heat transfer to heat diffusion.

Fig. 7 shows a plot of the ratio of enthalpies versus the Marangoni number for the 10 cases modeled and a clear transition that happens around $\Delta H/ h_s = 6$. This transition occurs near a Marangoni number of 1. Marangoni numbers higher than 1 indicate that the heat transfer in the melt pool becomes dominated by convection. King et al. [43] present a mathematical model that predicts transition from conduction melting to keyhole type melting at $\Delta H/ h_s = 6$. The data from this study clearly supports the idea that a transition occurs at this point. However, King et al. also present solutions from a numerical model which shows a transition to keyhole melting at $\Delta H/ h_s = 30$. The discrepancy in these values may be an indication that there is not a single specific point where this change occurs, rather the transition occurs gradually, over a range of values of normalized enthalpies. The discrepancy may also be due to differences in how keyhole melting is defined, whether is it simply geometric, in that keyhole melting occurs when the depth of the melt pool is greater than the width, or if it is defined by the presence of a vapor pocket, which requires significant vaporization to be occurring in the melt pool.

This transition region should be expected because as the energy input to the melt pool increases, the heat transfer in the melt pool is initially dominated by conduction, but as temperature gradients increase, Marangoni flow and buoyancy-driven flows will increase, leading to a convection dominant flow. This does not necessarily mean keyhole melting has been reached if it is defined as including a pocket of vapor. It is possible that this convection dominated flow, with small amounts of vaporization could result in melt pools with depth that exceed the width while not experiencing the vaporization required to create a keyhole. Melting that is dominated by vaporization, enough to create a pocket of vapor occurs at high values of normalized enthalpies [44]. In this type of melting a significant portion of the melt pool volume is made of metal vapor, which allows the laser energy to more easily penetrate into the melt pool and powder bed beneath [45]. A transition mode could exist where convection is the dominant heat transfer mode but the melt pool is still primarily made up of liquid metal, rather than vaporized metal (unlike keyhole melting).

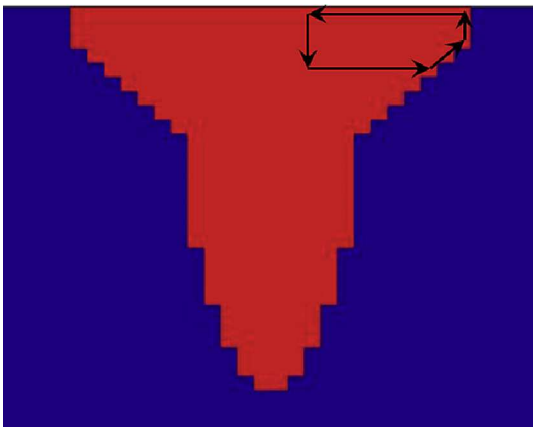

Fig. 8. The path used in calculating melt pool circulation.

According to *Le* and Lo [20] there is a transition region between the conduction mode and the keyhole melting mode for values of $\Delta H/ h_s$ from 30 to 75. Based on data from this study, it could be argued that this transition mode begins as early as $\Delta H/ h_s = 6$. The data presented by *Le* and Lo [20] include very little data below $\Delta H/ h_s = 30$, so it is possible that the transition begins earlier than *Le* and Lo are presenting. For this study, the cases of $\Delta H/ h_s > 6$, are likely in this transition region, as the Marangoni number is >1 (indicating significant convection), but the vaporization rates that were modeled and the values of $\Delta H/ h_s$ that are much lower than 75, indicate that these points are likely not experiencing keyhole melting.

Velocity and circulation were also examined in the model results. The maximum velocity in the X-direction varied from 0.3 m/s for the case of 50 W and 200 mm/s to 0.78 m/s for 150 W and 100 mm/s. As mentioned above, information on velocity magnitudes in melt pools is sparse in literature. Zhang et al. [19] reported a maximum velocity of 0.6 m/s for Inconel 718 at 400 W and 1200 mm/s scanning speed, which falls in the range of velocities predicted in this study.

Understanding the circulation that occurs inside the melt pool caused by surface tension gradients could provide insight into the motion of

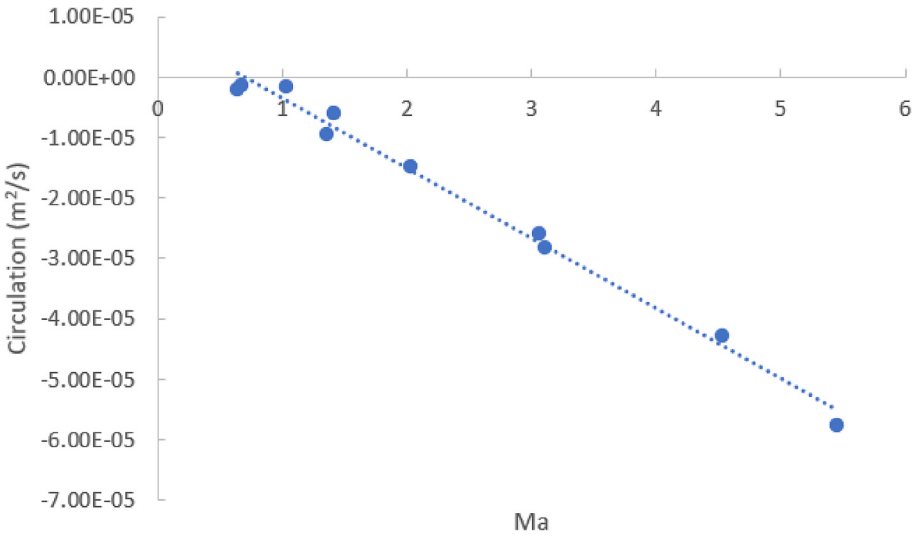

Fig. 9. Modeled results for circulation versus Marangoni number.

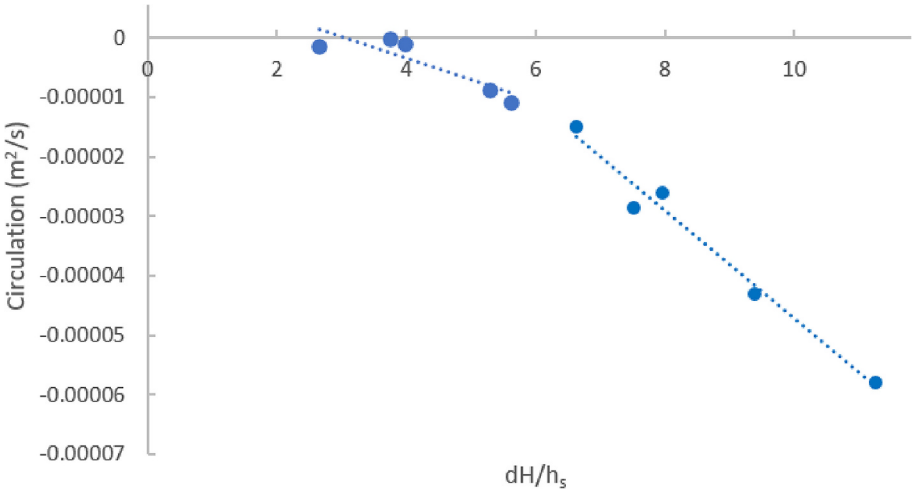

Fig. 10. Non-dimensional enthalpy versus circulation.

augmenting particles that are added to the powder bed to produce metal matrix composites. To empower designers with the ability to create functionally graded parts, the motion of the molten melt pool needs to be better understood, including circulatory flow. The circulation was calculated using MATLAB R2021b to postprocess velocity information from the ANSYS Fluent model for each sample. Fig. 8 shows the path that was used when calculating the circulation. It was expected that since the Marangoni number represents the ratio of convective to conductive heat transfer, as the Marangoni number increases, the magnitude of the circulation should also increase. This is because the circulation is caused by the Marangoni flow. Fig. 9 shows a plot of the circulation calculated for each case versus the Marangoni number.

By definition, circulation is calculated in a counter-clockwise manner, so it is reasonable for the selected path here the magnitude is negative. This indicates that on the positive x (right side) of the melt pool there is clockwise circulation induced by the Marangoni flow. The flanged shape at the top of the melt pool demonstrates that there is flow in that direction, pushing the edge of the melt pool toward the positive x direction. The magnitude of the circulation increases with increasing Marangoni number. A linear trend line was included on the plot to emphasize the apparent linear nature of the relationship between the circulation and the Marangoni number.

The effect of input energy (in terms of $\Delta H/ h_s$) was also examined as shown in Fig. 10. It can be seen from this data that, as mentioned before, there appears to be a transition that occurs near $\Delta H/ h_s = 6$.

To further provide information that will enable designers to create functionally graded materials, the information from the numerical model was used to predict the motion of particles added to the powder bed. Using velocity information for each time step, the movement of neutrally buoyant, non-reactive particles was predicted for each case. Supplementary video 1 is an animation of the motion viewed in the XY plane of these particles for the case of 150 W and 200 mm/s scanning speed.

Evidence of the circulatory flow induced by the surface tension gradients can be seen in the particle motion shown in Supplementary video 1. The particles start at the midpoint of the powder bed in the *Z*-direction. There is some motion in the positive or negative Z-direction, which is why near the end of the animation in Supplementary video 1 some particles are still in motion even though the midplane is no longer in a molten state. These particles move to parts of the powder bed where there is still molten metal causing motion. Supplementary video 2 is an animation of particle motion showing in the YZ plane, along the direction of travel of the laser, for the sample manufactured at 150 W and 200 mm/s. The particles in Supplementary video 2 are initially located at X = 0, which is the midplane in the X-direction.

There is evidence for circulatory flow in the YZ plane in the

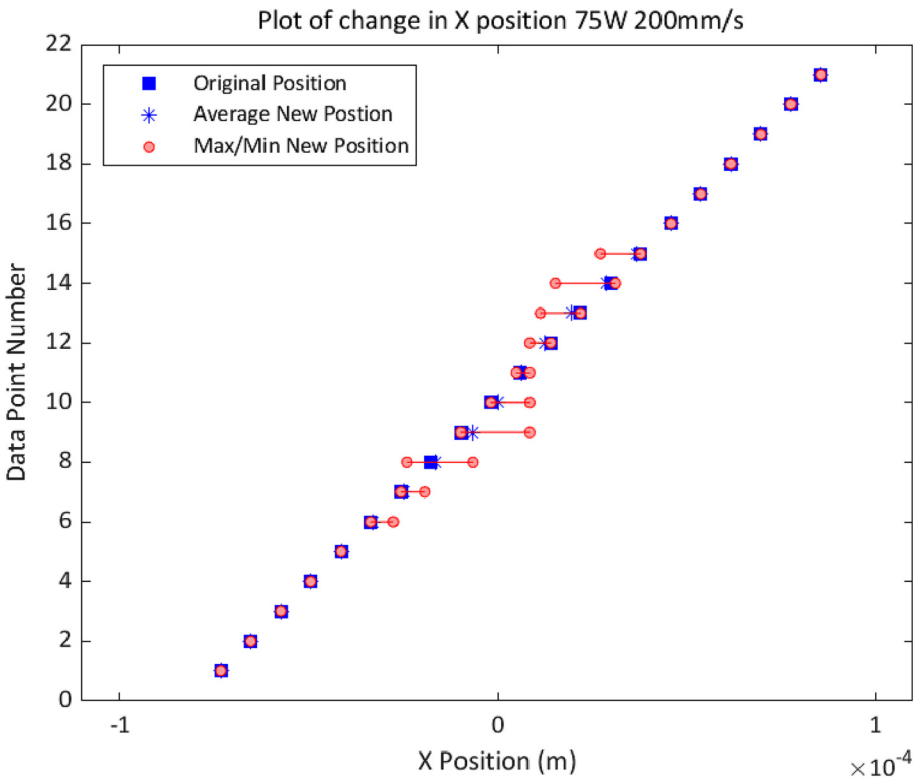

Fig. 11. The change in X Position for multiple starting locations for the case of 75 W and 200 mm/s.

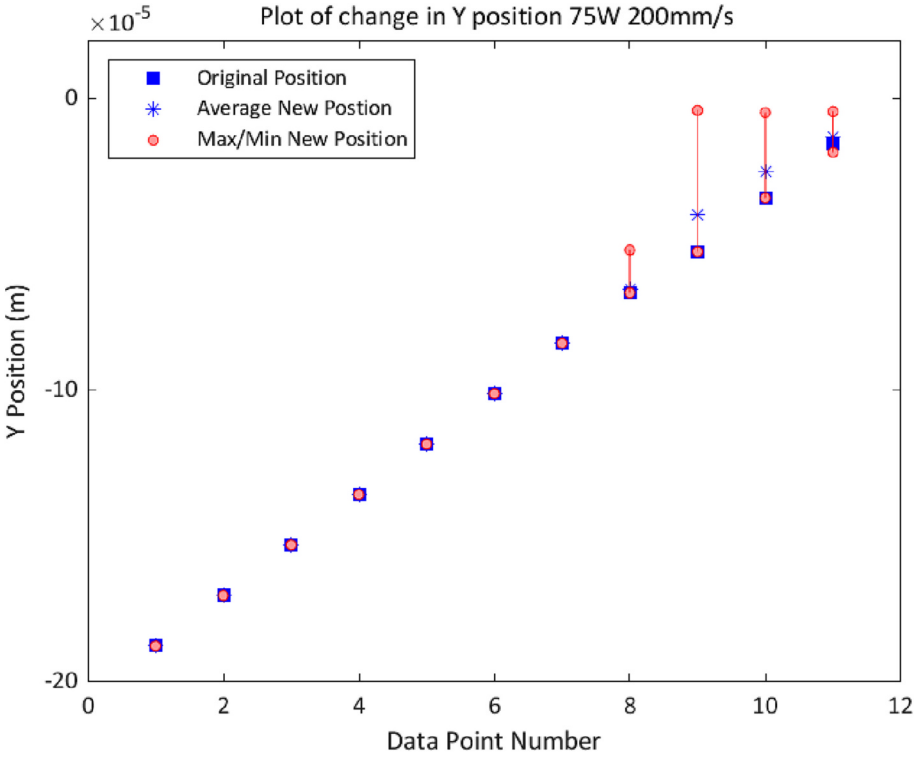

Fig. 12. The change in Y Position for multiple starting locations for the case of 75 W and 200 mm/s.

animation in Supplementary video 2. The fluid appears to circulate in an area in front of the laser, and separately behind the laser. A significant number of particles appear to become entrained in with the laser motion, likely caught in between these two different circulatory areas.

While these animations provide good qualitative information, they do not necessarily provide the quantitative data that would be needed for designing FGMs for LPBF. Figs. 11, 12, and 13 provide data on the average change in position for the particles in the X, Y, and Z directions

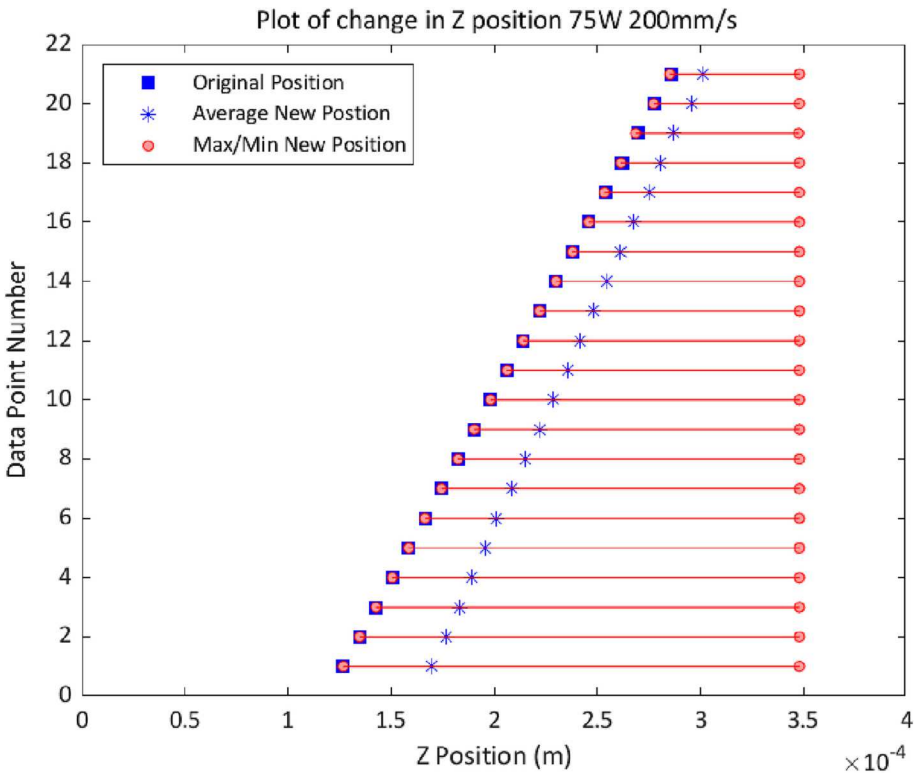

Fig. 13. The change in Z Position for multiple starting locations for the case of 75 W and 200 mm/s.

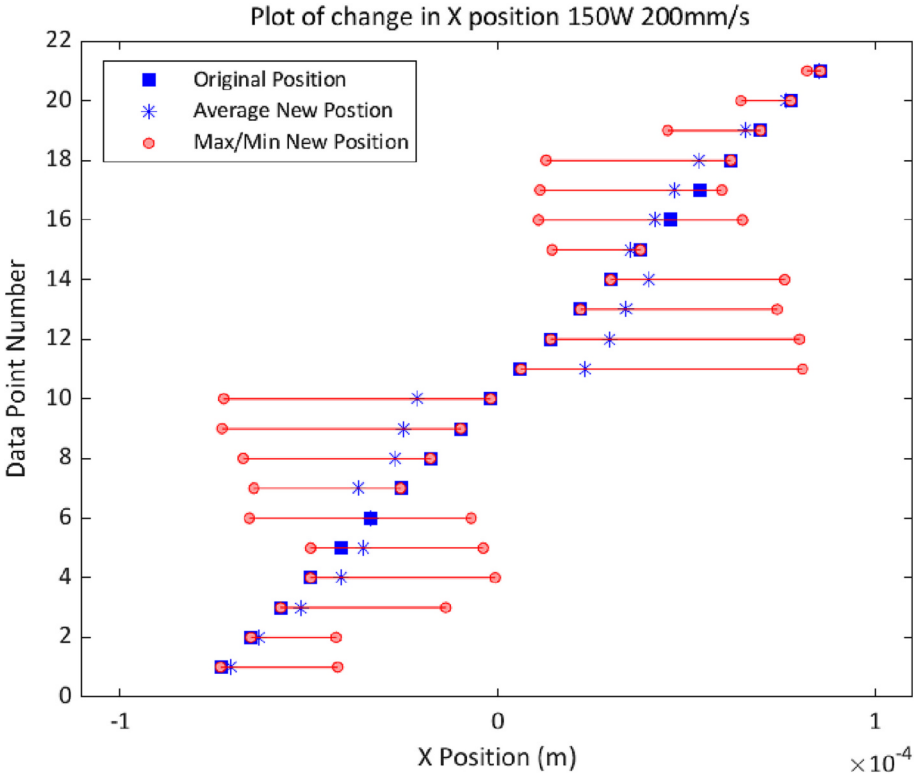

Fig. 14. The change in X Position for multiple starting locations for the case of 150 W and 200 mm/s.

respectively for the case of 75 W and 200 mm/s laser speed. Figs. 14, 15, and 16 have the same information for the case of 150 W, 200 mm/s. For plots of X and Y position, the data is taken from the same starting points as in Supplementary video 1, with several points at different X and Y locations at the midpoint of the model volume in the *Z*-direction. For the plots of Z position, the data is taken from the same starting points as shown in Supplementary video 2, with multiple starting points in Z and Y, taken at the midpoint of the volume in the X direction.

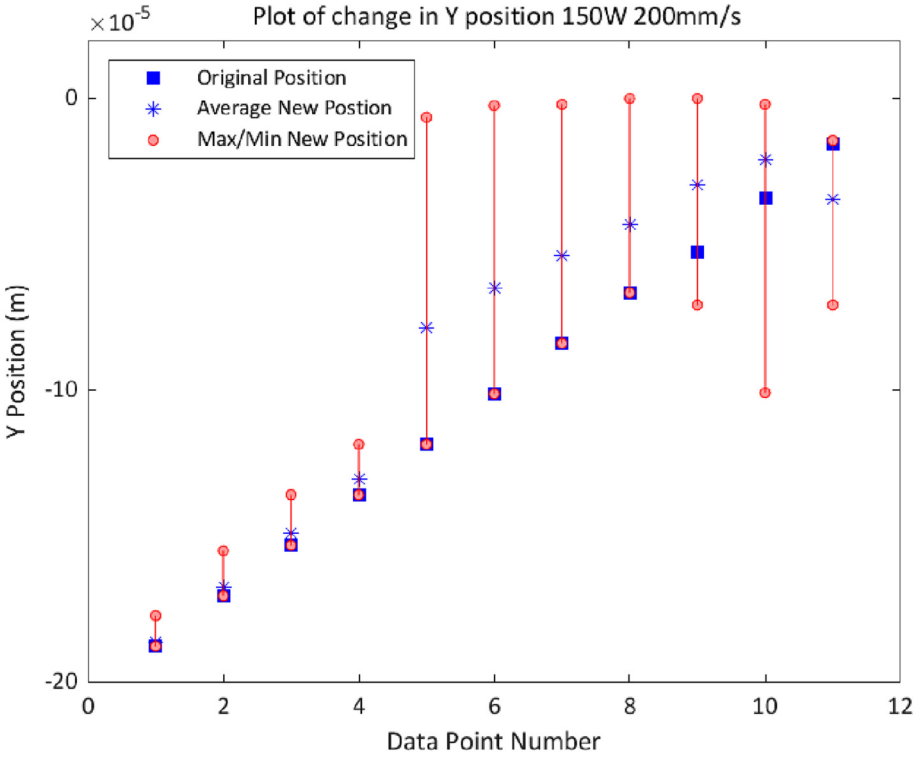

Fig. 15. The change in Y Position for multiple starting locations for the case of 150 W and 200 mm/s.

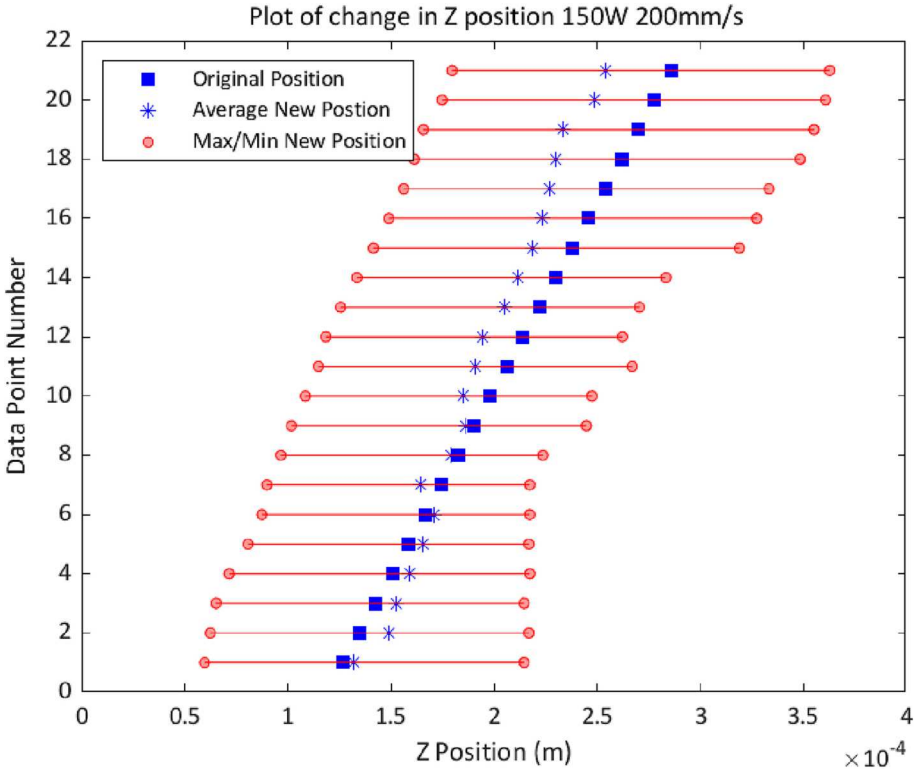

Fig. 16. The change in Z Position for multiple starting locations for the case of 150 W and 200 mm/s.

Figs. 17, 18, and 19 show the average change in position plotted against starting location for varying laser inputs in terms of $\Delta H/ h_s$ for all the cases that were modeled. For all of these cases the laser travels in the positive Z-direction, with the beam centered at X = 0. This data was taken with the same starting points as the previous plots.

In general, particles starting on the left of the laser beam (which is located near X = 0) tend to move in the negative X-direction. The Marangoni flow is directed out from the center of the laser, which on the

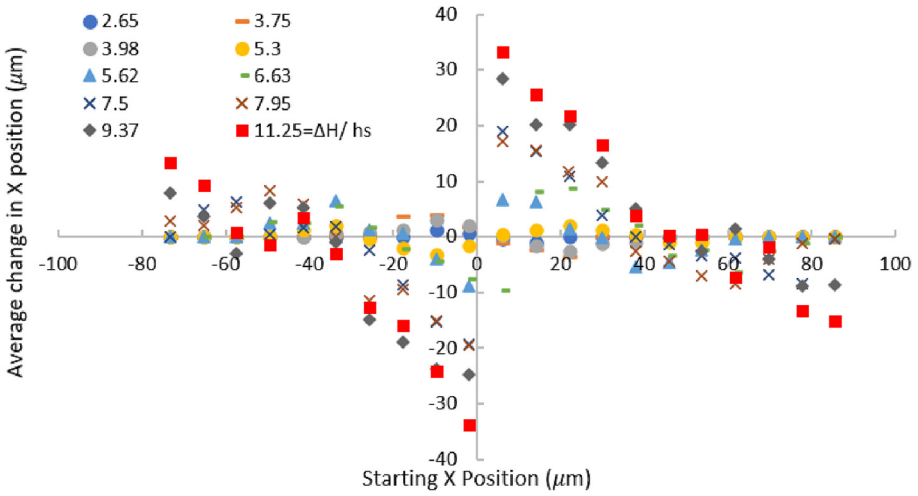

Fig. 17. The average change in position in the X-direction with varying values of ΔH/ h_s.

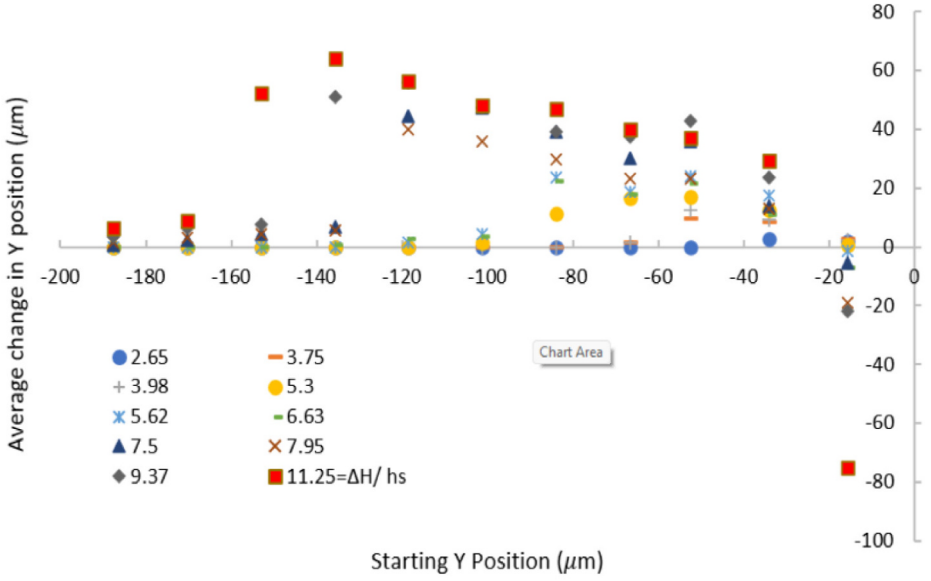

Fig. 18. The average change in position in the Y-direction with varying values of ΔH/ h_s.

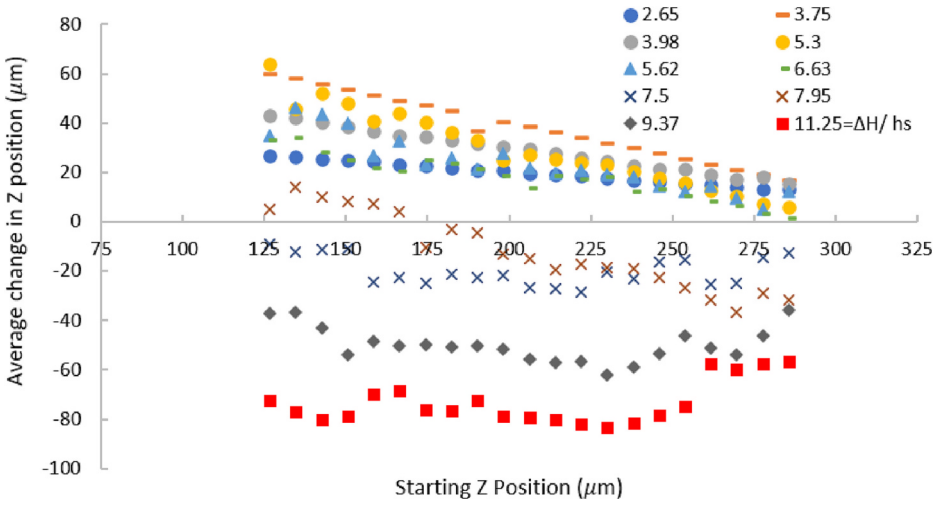

Fig. 19. The average change in position in the Z-direction with varying values of ΔH/ h_s.

Table 5
Results of varying the surface tension gradient.

	Case 1	Case 2	Case 3
dγ/dT (N/m-k)	-2.2×10^{-4}	-4.4×10^{-4}	2.2×10^{-4}
Melt Pool Width (μm)	167.2	197.6	91.2
Ma	3.07	5.38	0.97
Circulation	-2.65×10^{-5}	-4.47×10^{-5}	3.39×10^{-6}
ΔH/ds	7.95	7.95	7.95

negative X side would cause flow in that direction. While on the positive X side, the flow away from the laser would be in the positive X direction. The temperature gradients are largest near the laser, which is why particles that start near the center see the largest movement. Farther out from the laser beam the temperature gradients are smaller, and in turn the surface tension gradients are smaller, resulting in smaller change in position further out from the center of the laser. The magnitude of the change in position generally increases with increasing input power.

From Fig. 18 it can be seen that the average change in the Y direction for most locations in the melt pool is in the positive Y direction. This is due to both buoyancy and circulation caused by Marangoni flow creating a bulk motion upwards in the fluid. This motion is restricted, however, when particles reach the top of the melt pool. These particles that start near or reach the surface recirculate to fill in behind the upward flow to end up at a location deeper in the melt pool.

The data in Fig. 19 shows that for enthalpy ratios of <7.95 the average change in position is in the positive Z direction, the same direction that the laser travels. For enthalpy ratios >7.95, the travel in in the negative Z direction, moving behind and away from the laser. This occurs because at the higher energy inputs, there is Marangoni flow created in the *Z*-direction. At these increased energy input levels the area of molten material is relatively long, and this area behind the laser has a large temperature gradient. This causes flow behind the laser toward the lower temperatures, resulting in an average change in the negative Z-direction for these higher power cases. Clark et al. [26] provide some of the only data on motion in LPBF melt pools. Their work shows many tracer particles becoming entrained in the keyhole generated by the laser, with the particles conglomerating near the bottom of the pool, whereas this study shows particles generally rising up to the top of the melt pool. This difference is due to the density of the tungsten particles used by Clark et al. [26] being greater than the density of the copper-aluminum mixture in the powder bed. Whereas the particles in this study were neutrally buoyant and were able to follow with the fluid as it flowed upward from both the buoyancy that exists in the melt pool and the circulation caused by Marangoni flow.

As discussed earlier, this Marangoni flow is the main driver for the motion in melt pools that will affect the location of augmenting particles in functionally graded materials or metal matrix composites manufactured via the LPBF process. All of the cases discussed so far were simulated with a surface tension gradient (dγ/dT) of -2.2×10^{-4} N/m-k because it is close to the value used by Xiao and Zhang [45], and because it gave results that were validated with the experimental data. Wang and Tsai [46] reported that variations in the sulfur content of steels result in variations of the surface tension gradient. They found that increasing the sulfur content of the steel decreases the magnitude of the gradient, and past a certain point it would change the sign on the gradient from negative to positive. This gradient value directly affects Marangoni flow, so variations due to differences in chemical composition and trace elements (e.g, O, S, P) could result in different motion in molten melt pools.

To explore the effect that varying the surface tension gradient will have on LPBF the simulation in this study was run at three additional cases. The first was using one of the original cases, with a surface tension gradient of -2.2×10^{-4} N/m-k, with a laser power of 150 W and a scanning speed of 200 mm/s. The second case was run with the same laser power and scanning speed, but with the surface tension gradient doubled to -4.4×10^{-4} N/m-k. The third case was again done with the same laser parameters, but this time with a surface tension gradient of 2.2×10^{-4} N/m-k. Table 5 lists the results from these simulations.

Of these three cases examined, they all have the same heat input as the laser power and scanning speed are the same for all of these cases. Increasing the magnitude of the surface tension gradient resulted in an increased circulation, and increased Marangoni number. Switching the sign on the surface tension gradient resulted in a much lower Marangoni number, reduced circulation, and the sign of the circulation also switched, indicating that with a positive surface tension gradient the circulation in the melt pool will be in the counterclockwise direction, which agrees with the findings of Siao and Wen [18].

Fig. 20 shows the melt pool resulting for each case. Both cases with negative values of the surface tension coefficient have wide melt pools at the top, which is consistent with flow outward from the pushing the melt pool in that direction. For the case with the positive coefficient the flow generated from surface tension is inward toward the center of the laser, resulting in a different melt pool shape.

4. Conclusions

A numerical thermo-fluid model of the laser-power bed fusion process was developed to examine fluid motion in the melt pool during the process. The model was validated through comparison to experimental data and literature. Normalized enthalpies and a simplified Marangoni number were used to examine the results of the simulation. From the results it appears that a transition occurs near $\Delta H/h_s = 6$ and Marangoni numbers >1. This transition is likely not the start of keyhole type melting because the heat input and the vaporization rates are lower than expected for keyhole type melting. Rather, it appears to be the beginning of a transition mode where the heat transfer in the melt pool is dominated by convection of the molten metal, but keyhole melting is not yet achieved. The magnitude of the circulation in the melt pool was calculated and it was found to have a linear relationship with the Marangoni number. The position of several neutrally buoyant and non-reactive

Fig. 20. Melt pools with varying surface tension coefficients, left is -2.2×10^{-4} N/m-k, center -4.47×10^{-5}, and right is 2.2×10^{-4}.

particles was tracked as they move with the fluid motion in the powder bed during LPBF. Additive manufacturing of metal matrix composites and functionally graded parts via hybrid ink-jetting and LPBF will depend on understanding of the motion these augmenting particles will undergo during the process. The information in this study provides insights into potential motion of these particles based on multiple different starting locations in the powder bed.

CRediT authorship contribution statement

Bryce Cox: Methodology, Software, Validation, Data curation, Writing – original draft, Visualization. **Milad Ghayoor:** Investigation, Data curation, Writing – review & editing. **Somayeh Pasebani:** Supervision, Resources, Writing – review & editing, Funding acquisition. **Joshua Gess:** Conceptualization, Resources, Writing – review & editing, Project administration, Supervision.

Declaration of Competing Interest

The authors declare that they have no known competing financial interests or personal relationships that could have appeared to influence the work reported in this paper.

Data availability

Data will be made available on request.

Acknowledgments

The authors gratefully acknowledge the financial support of the National Science Foundation Advanced Manufacturing Program through Award Number 1856412. Any findings and conclusions are those of the authors and do not necessarily reflect the views of the National Science Foundation. The authors would also like to acknowledge the funding of critical equipment provided by the Murdock Charitable Trust (contract number: 2016231:MNL:5/18/2017), the RAPID Institute, and the U.S. DOE (contract number: DE-EE0007888). MG and SP thank Dr. Peter Eschbach at OSU electron microscopy center, Ryan P. Doyle, ATAMI staff, especially Nick Warrenmacher.

Appendix A. Supplementary data

Supplementary data to this article can be found online at https://doi.org/10.1016/j.powtec.2023.118610.

References

[1] T. DebRoy, H.L. Wei, J.S. Zuback, T. Mukherjee, J.W. Elmer, J.O. Milewski, A. M. Beese, A. Wilson-Heid, A. De, W. Zhang, Additive manufacturing of metallic components - process, structure and properties, Prog. Mater. Sci. 92 (C) (2018) 112–224, https://doi.org/10.1016/j.pmatsci.2017.10.001.
[2] Itziar Tolosa, Fermín Garciandía, Fidel Zubiri, Fidel Zapirain, Aritz Esnaola, Study of mechanical properties of AISI 316 stainless steel processed by "selective laser melting", following different manufacturing strategies, Int. J. Adv. Manuf. Technol. 51 (5) (2010) 639–647, https://doi.org/10.1007/s00170-010-2631-5.
[3] Valmik Bhavar, Prakash Kattire, Sandeep Thakare, S. Patil, D.R. Singh, A review on functionally graded materials, Int. J. Eng. Sci. (IJES) 3 (2014) 90.
[4] J.-H. You, et al., Thermal and mechanical properties of infiltrated W/CuCrZr composite materials for functionally graded heat sink application, J. Nucl. Mater. 438 (1–3) (2013) 1–6.
[5] Antonella Sola, et al., Functionally graded materials for orthopedic applications - an update on design and manufacturing, Biotechnol. Adv. 34 (5) (2016) 504–531.
[6] V.E. Beal, P. Erasenthiran, C.H. Ahrens, P. Dickens, Evaluating the use of functionally graded materials inserts produced by selective laser melting on the injection moulding of plastics parts, Proc. Inst. Mech. Eng. B J. Eng. Manuf. 221 (6) (2007) 945–954.
[7] S.W. Sing, J. An, W.Y. Yeong, F.E. Wiria, Laser and electron-beam powder-bed additive manufacturing of metallic implants: a review on processes, Mater. Des. Orthop. Res. 34 (2015) 369–385.
[8] Dongdong Gu, et al., Selective laser melting additive manufacturing of Ti-based nanocomposites: the role of nanopowder, Metall. Mater. Trans. A Phys. Metallu. Mater. Sci. 45 (1) (2014) 464–476.
[9] Dongdong Gu, et al., Densification behavior, microstructure evolution, and Wear property of TiC nanoparticle reinforced AlSi10Mg bulk-form nanocomposites prepared by selective laser melting, J. Laser Appl. 27 (S1) (2015) S17003.
[10] Y.S. Lee, W. Zhang, Modeling of heat transfer, fluid flow and solidification microstructure of nickel-base superalloy fabricated by laser powder bed fusion, Addit. Manuf. 12, no. B (2016) 178–188.
[11] F. Verhaeghe, et al., A pragmatic model for selective laser melting with evaporation, Acta Mater. 57 (20) (2009) 6006–6012.
[12] Zhenglong Lei, et al., Numerical study of thermal fluid dynamics in laser welding of Al alloy with powder feeding, Appl. Therm. Eng. 151 (2019) 394–405.
[13] Nissar Ahmed, Imad Barsoum, G. Haidemenopoulos, R. Al-Rub, Process parameter selection and optimization of laser powder bed fusion for 316L stainless steel: A review, J. Manuf. Process. 75 (2022) 415–434, https://doi.org/10.1016/j.jmapro.2021.12.064.
[14] E.L. Papazoglou, et al., A comprehensive study on thermal modeling of SLM process under conduction mode using FEM, Int. J. Adv. Manuf. Technol. 111 (9–10) (2020) 2939–2955.
[15] Claire Bruna-Rosso, Ali Gökhan Demir, Barbara Previtali, Selective laser melting finite element modeling: validation with high-speed imaging and lack of fusion defects prediction, Mater. Des. 156 (2018) 143–153, https://doi.org/10.1016/j.matdes.2018.06.037.
[16] John Goldak, Aditya Chakravarti, Malcolm Bibby, A new finite element model for welding heat sources, Metall. Trans. B 15 (2) (1984) 299–305, https://doi.org/10.1007/BF02667333.
[17] Saad A. Khairallah, Andy Anderson, Mesoscopic simulation model of selective laser melting of stainless steel powder, J. Mater. Process. Technol. 214 (11) (2014) 2627–2636.
[18] Yong-Hao Siao, Chang-Da Wen, Examination of molten pool with Marangoni flow and evaporation effect by simulation and experiment in selective laser melting, Int. Commun. Heat Mass Transfer 125 (2021), 105325, https://doi.org/10.1016/j.icheatmasstransfer.2021.105325.
[19] Dongyun Zhang, Pudan Zhang, Zhen Liu, Zhe Feng, Chengjie Wang, Yanwu Guo, Thermofluid field of molten pool and its effects during selective laser melting (SLM) of Inconel 718 alloy, Addit. Manuf. 21 (2018) 567–578, https://doi.org/10.1016/j.addma.2018.03.031.
[20] Trong-Nhan Le, Yu-Lung Lo, Effects of sulfur concentration and Marangoni convection on melt-pool formation in transition mode of selective laser melting process, Mater. Des. 179 (2019), 107866, https://doi.org/10.1016/j.matdes.2019.107866.
[21] Tao Zhang, et al., Evolution of molten pool during selective laser melting of Ti-6Al-4V, J. Phys. D, Appl. Phys. 52 (5) (2018) 55302.
[22] Thorsten Heeling, Michael Cloots, Konrad Wegener, Melt pool simulation for the evaluation of process parameters in selective laser melting, Addit. Manuf. 14 (2017) 116–125, https://doi.org/10.1016/j.addma.2017.02.003.
[23] Qian Ye, Shikui Chen, Numerical modeling of metal-based additive manufacturing using level set methods, J. Manuf. Sci. Eng. 139 (7) (2017), https://doi.org/10.1115/1.4036290.
[24] Anderson Khairallah, A. T., Rubenchik, A., & King, W. E., Laser powder-bed fusion additive manufacturing: physics of complex melt flow and formation mechanisms of pores, spatter, and denudation zones, Acta Mater. 108 (C) (2016) 36–45, https://doi.org/10.1016/j.actamat.2016.02.014.
[25] Berg Tenner, B., Brock, C., Klämpfl, F., & Schmidt, M., Experimental approach for quantification of fluid dynamics in laser metal welding, J. Laser Appl. 27 (S2) (2015), https://doi.org/10.2351/1.4906302. S29003.
[26] S.J. Clark, C.L.A. Leung, Y. Chen, L. Sinclair, S. Marussi, P.D. Lee, Capturing Marangoni flow via synchrotron imaging of selective laser melting. IOP conference series, Mater. Sci. Eng. 861 (1) (2020) 12010, https://doi.org/10.1088/1757-899X/861/1/012010.
[27] Uemura Y. Kawahito, Y. Doi, M. Mizutani, K. Nishimoto, H. Kawakami, M. Tanaka, H. Fujii, K. Nakata, S. Katayama, Elucidation of the effect of welding speed on melt flows in high-brightness and high-power laser welding of stainless steel on basis of three-dimensional X-ray transmission in situ observation, Weld. Int. 31 (3) (2017) 206–213, https://doi.org/10.1080/09507116.2016.1223204.
[28] Zhao C. Guo, M. Qu, L. Xiong, S.M.H. Hojjatzadeh, L.I. Escano, N.D. Parab, K. Fezzaa, T. Sun, L. Chen, In-situ full-field mapping of melt flow dynamics in laser metal additive manufacturing, Addit. Manuf. 31 (C) (2020), https://doi.org/10.1016/j.addma.2019.100939, 100939.
[29] R.C. Crafer, P.J. Oakley, Laser Processing in Manufacturing, 1st ed., Chapman & Hall, 1993.
[30] X. Wang, T. Laoui, J. Bonse, J. Kruth, B. Lauwers, L. Froyen, Direct selective laser sintering of hard metal powders: experimental study and simulation, Int. J. Adv. Manuf. Technol. 19 (5) (2002) 351–357.
[31] J. Trapp, A. Rubenchik, G. Guss, M. Matthews, et al., In situ absorptivity measurements of metallic powders during laser powder-bed fusion additive manufacturing, Appl. Mater. Today 9 (2017) 341–349.
[32] M. Gunther, N. Susanna, J. Simon, M. Christiane, H. Kai, Experimental determination of the emissivity of powder layers and bulk material in laser powder bed fusion using infrared thermography and thermocouples, Metals (Basel) 10 (1546) (2020) 1546.
[33] H. Fukuyama, H. Higashi, H. Yamano, Thermophysical properties of molten stainless steel containing 5 mass % B4C, Nucl. Technol. 205 (9) (2019) 1154–1163.
[34] Xiao, Y. Zhang, Numerical simulation of direct metal laser sintering of single-component powder on top of sintered layers, J. Manuf. Sci. Eng. 130 (4) (2008), https://doi.org/10.1115/1.2951948, 041002 (10)–041002 (10).
[35] Powder Metallurgy Stainless Steels; Processing, Microstructures, and Properties vol. 31, no. 4, SciTech Book News, 2007, 2007–12-01.

[36] C. Kim, Thermophysical Properties of Stainless Steels Argonne National Laboratory, Lemont, IL, United States, 1975 (Technical Report ANL-75-55.).
[37] Ghayoor M. Cox, R.P. Doyle, S. Pasebani, J. Gess, Numerical model of heat transfer during laser powder bed fusion of 316L stainless steel, Int. J. Adv. Manuf. Technol. 119 (9–10) (2022) 5715–5725, https://doi.org/10.1007/s00170-021-08352-0.
[38] T. Zhang, H. Li, S. Liu, S. Shen, H. Xie, W. Schi, G. Zhang, B. Shen, L. Chen, B. Xiao, M. Wei, Evolution of molten pool during selective laser melting of Ti-6Al-4V, J. Phys. D, Appl. Phys. 52 (5) (2018) 55302.
[39] T.C. Chawla, D.L. Graff, R.C. Borg, G.L. Bordner, D.P. Weber, D. Miller, Thermophysical properties of mixed oxide fuel and stainless steel type 316 for use in transition phase analysis, Nucl. Eng. Des. 67 (1981) 57–74.
[40] Meneghello Ferro, R., Savio, G., & Berto, F., A modified volumetric energy density–based approach for porosity assessment in additive manufacturing process design, Int. J. Adv. Manuf. Technol. 110 (7–8) (2020) 1911–1921, https://doi.org/10.1007/s00170-020-05949-9.
[41] Ramirez-Cedillo E. Uddin, R.A. Mirshams, H.R. Siller, Nanoindentation and electron backscatter diffraction mapping in laser powder bed fusion of stainless steel 316L, Mater. Charact. 174 (2021), 111047, https://doi.org/10.1016/j.matchar.2021.111047.
[42] Chen C. Zhao, W. Wang, T. Cao, S. Shuai, S. Xu, T. Hu, H. Liao, J. Wang, Z. Ren, On the role of volumetric energy density in the microstructure and mechanical properties of laser powder bed fusion Ti-6Al-4V alloy, Addit. Manuf. 51 (2022), https://doi.org/10.1016/j.addma.2022.102605.
[43] Barth H.D. King, V.M. Castillo, G.F. Gallegos, J.W. Gibbs, D.E. Hahn, C. Kamath, A. M. Rubenchik, Observation of keyhole-mode laser melting in laser powder-bed fusion additive manufacturing, J. Mater. Process. Technol. 214 (12) (2014) 2915–2925, https://doi.org/10.1016/j.jmatprotec.2014.06.005.
[44] Garmestani Wang, H., & Liang, S. Y., Prediction of molten pool size and vapor depression depth in keyhole melting mode of laser powder bed fusion, Int. J. Adv. Manuf. Technol. 119 (9–10) (2022) 6215–6223, https://doi.org/10.1007/s00170-021-08295-6.
[45] Zhou Z. Li, L. Wang, R. Zou, A. Yu, Modelling of keyhole dynamics and melt pool flow in laser powder bed fusion process, Powder Technol. 400 (2022), https://doi.org/10.1016/j.powtec.2022.117262.
[46] Wang, H.L. Tsai, Effects of surface active elements on weld pool fluid flow and weld penetration in gas metal arc welding. Metallurgical and materials transactions. B, process metallurgy and materials processing, Science 32 (3) (2001) 501–515, https://doi.org/10.1007/s11663-001-0035-5.